Dual-Site Coordination Regulated Crystallization for High-Performance MAPbBr3X-Ray Detectors

Authors: Zhang, Dr. Yue, Sun, Dr. Yuanjie, Zhe Liu, Zhao, Mr. Huatong, Prof. Hongtao Zhao, Li, Dr. Zhigang, Zhao, Prof. Hongtao

Date: 2025-11-24T00:00:00+00:00

Abstract

Organic-inorganic hybrid perovskite single crystals have shown great potential as next-generation high-sensitivity X-ray detectors. However, the thermodynamic instability of their precursor solutions often leads to disordered nucleation and defect proliferation during crystallization, which considerably limits the performance of resulting devices. This study shows that polymeric inhibitor effectively suppresses disordered nucleation in perovskite precursor solutions. The coordination mechanism between PVP and the MAPbBr3 precursor solutions is revealed by IGMH (Independent Gradient Model based on Hirshfeld partition) analysis, density functional theory (DFT) calculations, and experimental results. It is revealed that PVP forms a distinct dual-site coordination complex with Pb2+ , interacting simultaneously through its carbonyl and pyrrolidone ring. This specific coordination geometry significantly enhances the thermodynamic stability of the precursor system by maintaining an optimal solute concentration within the metastable zone, thus effectively inhibiting spontaneous nucleation. The MAPbBr3 (with PVP) SC exhibits a low defect density of 6.56×108 cm-3 and a high carrier mobility-lifetime product ( ) of 1.11×10-3 cm2 • V-1. The X-ray detector fabricated based on the crystal demonstrates a high sensitivity of 1.73×104 C • Gyair-1 • cm-2 and a low detection limit of 43.55 nGyair-1 • s-1. This study provides a new strategy for modulating perovskite crystallization kinetics through coordination engineering, offering a viable pathway for developing high-performance radiation detectors.

Full Text

Dual-Site Coordination Regulated Crystallization for High-Performance MAPbBr3 X-Ray Detectors

Yue Zhang[1], Yuanjie Sun[1], Zhe Liu[2], Huatong Zhao[3], Hongtao Zhao[1,2,3,*], Zhigang Li[2,*]

[1]College of Physics and Optoelectronic Engineering, Harbin Engineering University, Harbin 150001, China
[2]Key Laboratory of Advanced Materials and Devices, Harbin Engineering University, Harbin 150001, China
[3]Institute of Advanced Materials and Technology, Heilongjiang Academy of Sciences, Harbin 150001, China

*Email: zhaohongtao@hrbeu.edu.cn (Hongtao Zhao); lzg0015@hrbeu.edu.cn (Zhigang Li)

Abstract

Organic-inorganic hybrid perovskite single crystals have emerged as promising candidates for next-generation high-sensitivity X-ray detectors. However, the thermodynamic instability of their precursor solutions often leads to disordered nucleation and defect proliferation during crystallization, which severely limits device performance. This study demonstrates that a polymeric inhibitor effectively suppresses disordered nucleation in perovskite precursor solutions. The coordination mechanism between polyvinylpyrrolidone (PVP) and MAPbBr3 precursor solutions was elucidated through Independent Gradient Model based on Hirshfeld partition (IGMH) analysis, density functional theory (DFT) calculations, and experimental validation. Our findings reveal that PVP forms a distinct dual-site coordination complex with Pb^{2} , simultaneously interacting through its carbonyl group and pyrrolidone ring. This specific coordination geometry significantly enhances the thermodynamic stability of the precursor system by maintaining optimal solute concentration within the metastable zone, thereby effectively inhibiting spontaneous nucleation. The resulting MAPbBr single crystal (with PVP) exhibits a low defect density of 6.56×10 cm^{-3} and a high carrier mobility-lifetime product ( ) of 1.11×10^{-3} $cm^{2}\cdot V^{-1}$. The fabricated X-ray detector demonstrates exceptional performance with a sensitivity of 1.73×10 $C\cdot Gy^{-1}\cdot cm^{-2}$ and a low detection limit of 43.55 $nGy\cdot s^{-1}$. This work provides a novel strategy for modulating perovskite crystallization kinetics through coordination engineering, offering a viable pathway for developing high-performance radiation detectors.

Keywords: MAPbBr , Crystal growth, Dual-Site, Polymers, X-ray Detector

1. Introduction

Organic-inorganic hybrid perovskites have attracted considerable attention due to their remarkable performance in diverse applications including solar cells [**?**], photodetectors [**?**], and light-emitting diodes [**?**]. These materials show particularly promising potential for high-energy radiation detection because their constituent heavy elements, such as lead (Pb), confer strong radiation attenuation capabilities and enable efficient absorption of X-ray [**?**] and -ray photons [**?**]. Under X-ray irradiation, the carrier concentration generated in perovskites is substantially lower than that under solar illumination, placing stringent demands on defect reduction and charge transport properties [**?**]. Consequently, superior charge transport characteristics and minimized defect densities are essential requirements for perovskite-based X-ray detection applications.

To make perovskites viable for X-ray detection, their properties must be optimized to address these challenges. Previous studies have demonstrated that achieving high-quality crystals with reduced defect densities and enhanced charge transport is crucial [**?**]. Recent efforts have focused on modifying the crystallization process using polymers, which can effectively regulate perovskite film formation. Long-chain polymers, in particular, promote the formation of larger grains and passivate grain boundary defects through cross-linking interactions between their repeating units and perovskite precursors [**?**]. For example, poly(methyl methacrylate) (PMMA) retards crystal growth by forming intermediate complexes with PbI , thereby producing polycrystalline films with superior smoothness, reduced defect density, and enlarged grain size [**?**]. In another approach, carboxymethyl chitosan (CMC) was introduced, whereby its carboxyl groups chelate Pb^{2} ions to induce controlled nucleation and enhance film quality [**?**]. Meanwhile, dimethyl itaconate (DI) functions as a Lewis base by coordinating with PbI , and subsequent thermal polymerization generates steric hindrance that facilitates FAI intercalation and improves crystallization kinetics [**?**].

Despite promising results with polycrystalline materials, perovskite single crystals offer superior performance for X-ray detection due to their higher carrier mobility, longer recombination lifetimes, reduced ion migration, and improved stability—all stemming from the elimination of grain boundaries and defects [**?**, **?**]. Although solution-growth methods such as temperature lowering [**?**], antisolvent vapor-assisted crystallization [**?**], and slow evaporation [**?**] are commonly used to produce single crystals, they often suffer from prolonged processing times, difficulty in controlling nucleation, and challenges with crystal size and defect density. Elevated supersaturation levels typically induce excessive nucleation, restricting crystal growth and leading to defect formation [**?**]. Building on polymer-mediated nucleation control strategies, researchers have utilized polyacrylic acid (PAA) to coordinate with Pb^{2} via carboxyl groups, effectively suppressing the formation of Pb-I nuclei and reducing nucleation density. This approach has enabled the successful synthesis of high-quality MAPbI single crystals larger than 5 mm, significantly improving both crystalline quality and

stability [**?**]. Although polymer-mediated strategies have demonstrated considerable potential, current studies remain largely focused on polymer systems with single functional sites. In-depth investigations into dual-functional-site polymers and their underlying mechanisms remain relatively scarce.

To address these challenges, we propose a novel approach based on a bidentate ligand-assisted inverse temperature crystallization (ITC) method, incorporating polyvinylpyrrolidone (PVP, Mw: 58,000) into the perovskite precursor solution. PVP, with its carbonyl group and pyrrolidone ring, effectively coordinates with Pb^{2} ions during nucleation, reducing the formation of Pb-Br octahedral nuclei and limiting the diffusion rate of solute molecules. This coordination stabilizes the solution and reduces nucleation density, ultimately facilitating the growth of high-quality MAPbBr single crystals. The resulting single crystals exhibit significantly improved quality, with a 3.47-fold reduction in defect density and substantially reduced ion migration. Furthermore, X-ray detectors based on these MAPbBr single crystals show promising performance, achieving a stable sensitivity of 1.73×10 C·Gy ^{1}·cm ^{2} and a low detection limit of 43.55 nGy · s ^{1}. In conclusion, the bidentate ligand-assisted ITC method using PVP offers a highly effective strategy for fabricating high-quality perovskite single crystals, representing a significant advance in the development of high-performance X-ray detectors and providing a foundation for further advancements in radiation detection technologies.

---

2. Materials and Methods

Materials. Methylammonium bromide (MABr, 99.5%) was purchased from Xi' an Polymer Light Technology Corp. Lead bromide (PbBr , 99.0%), polyvinylpyrrolidone (PVP, Mw 58,000), and N,N-dimethylformamide (DMF, 98.5%) were obtained from Shanghai Aladdin Biochemical Technology Co., Ltd.

Synthesis of MAPbBr Single Crystals. A 0.15 M MAPbBr precursor solution was prepared by dissolving PbBr (0.15 M), MABr (0.15 M), and PVP (0.1 g) in 10 mL of DMF. The mixture was stirred at room temperature for 8 hours to ensure complete dissolution and subsequently filtered through a 0.22 m organic syringe filter. For nucleation-assisted growth, the solution was placed in a heating furnace and slowly heated to 65 ℃ in a single step at a rate of 2 ℃/h.

IGMH Analysis. The Independent Gradient Model based on Hirshfeld partition [**?**] represents a significant improvement over the conventional Independent Gradient Model (IGM). It optimizes the graphical representation of weak interactions by employing the Hirshfeld partition of the actual molecular electron density. Integrated into the MultiWFN [**?**] wavefunction analysis software, it enables in-depth exploration of both intermolecular weak interactions and chemical bonding interactions.

DFT Calculations. DFT calculations were performed using the ORCA program [**?**]. Molecular geometries were optimized at the B3LYP [**?**]-D3(BJ) [**?**]/def2-TZVP [**?**] level. CM5 atomic charges were computed using MultiWFN [**?**]. Frequency analysis confirmed the absence of imaginary frequencies, indicating that the optimized structures correspond to local minima on the potential energy surface. Single-point energy calculations were then carried out on the optimized geometries at the PWPB95 [**?**]-D3(BJ)/def2-QZVPP [**?**] level. Solvation free energies in DMF were computed using the uESE model [**?**]. The Gibbs free energies for the systems across the temperature range of 298.15 K to 353.15 K were calculated using the Shermo program [**?**] with the rigid rotor harmonic oscillator (RRHO) model [**?**], applying a vibrational scaling factor of 0.985. Finally, the changes in Gibbs free energy (ΔG) for the reactions were determined.

Solubility Test of MAPbBr . MAPbBr powder for solubility testing was prepared by grinding as-grown single crystals. A small amount of the powder was dissolved in a vial containing 10 mL of DMF. The vial was placed in an oil bath and heated to a predetermined temperature, with additional MAPbBr powder introduced in 0.02 mg increments during stirring. The solution was regarded as fully saturated when no further dissolution of trace solute was observed after 20 minutes of stirring following the final addition. This procedure was repeated at different temperatures to obtain the solubility curve.

Characterization. The crystal structure of MAPbBr single crystals was characterized by X-ray diffraction (Bruker Smart Apex, Cu K radiation). Photoluminescence spectra were acquired using a Raman-fluorescence hybrid system (Horiba LabRAM HR Evolution) with a xenon lamp excitation source at 365 nm. Time-resolved photoluminescence (TRPL) measurements were performed on an Edinburgh FLS980 spectrometer. The space-charge-limited current (SCLC) characteristics were measured to quantify the defect density and charge transport properties of the single-crystal perovskite samples. The dark I-V curve was measured using a semiconductor parameter analyzer (Agilent B1500A).

X-Ray Detector Performance. The X-ray detection performance was measured in a shielded dark box to minimize electromagnetic and ambient light interference. The X-ray source was generated by an X-ray tube (VF-50J-Rh) operated at 50 kV. The tube current was adjusted from 1000 A to 1 A to modulate the X-ray dose rate. An 8 mm-thick aluminum filter was used as an attenuator to shape the X-ray spectrum. The X-ray dose rate was calibrated using a calibrated dosimeter. The X-ray response current was recorded using a digital source meter (Keithley 2400).

---

3. Results and Discussion

The single-crystal growth temperature dictates the thermodynamic stability of the precursor solution system and the crystal growth rate, thereby influencing

both nucleation density and crystalline quality. To better illustrate the nucleation process of MAPbBr single crystals, Figure 1a [FIGURE:1] presents the nucleation temperature (N-T) and solubility temperature (S-T) curves of MAPbBr . These two curves divide the diagram into three distinct regions: the unsaturated zone (below the S-T curve, where spontaneous nucleation does not occur within the solubility limit), the metastable zone (between the N-T and S-T curves, where nucleation is followed by crystal growth without exceeding the nucleation threshold, enabling continuous crystal growth), and the unstable zone (above the N-T curve, where both thermodynamic and kinetic criteria are met, leading to spontaneous formation of numerous nuclei and thus limiting the growth of large single crystals).

Therefore, to obtain high-quality, large-sized single crystals, it is essential to maintain the solution concentration within the metastable zone (slightly below the N-T curve). As shown in Fig. 1a, for the MAPbBr precursor solution under high-temperature conditions, the simultaneous occurrence of nucleation and growth causes a sharp decline in solute concentration, resulting in entry into the unsaturated zone and consequent cessation of crystal growth. Throughout the entire crystallization process, the MAPbBr (with PVP) precursor solution consistently maintains its composition within the metastable zone, thereby enabling the successful acquisition of high-quality single crystals.

In perovskite precursor solutions, colloidal particles coexist with perovskite precursor ions [**?**]. Upon adding PVP to the MAPbBr precursor solution, PVP coordinates with the surface of these colloids. To clarify the microscopic interaction mechanism between PVP and the MAPbBr precursor solution, dynamic light scattering (DLS) and Fourier-transform infrared spectroscopy (FTIR) were employed for characterization. As presented in Fig. 1b, DLS measurements reveal that the average colloidal size in the MAPbBr /DMF precursor solution is approximately 1.11 nm. Following PVP introduction, the colloidal size increases to 1.68 nm. This size enlargement indicates the formation of complex clusters between the PbBr precursor and PVP, which reduces the concentration of free PbBr ^{2} species in the MAPbBr /DMF solution.

The coordination interaction between PVP and the MAPbBr precursor was further confirmed by FTIR spectroscopy. As shown in Fig. 1c, the peak observed at 1668 cm ^{1} is attributed to the C=O stretching vibration of PVP, while the peak at 1288 cm ^{1} corresponds to the C-N stretching vibration in the pyrrolidone ring [**?**]. In the PVP-MABr system, the electron cloud density of the C=O bond remains unchanged, with no discernible shift in peak position relative to pure PVP. For the PVP-PbBr complex, FTIR analysis reveals that Pb^{2} , acting as a strong Lewis acid, forms a coordination bond with the carbonyl oxygen, inducing a shift of the C=O peak to 1633 cm ^{1}. The downshift of the C-N peak to 1281 cm ^{1} indicates a weak coordination interaction between Pb^{2} and the lone electron pair on the nitrogen atom. In the MABr-PbBr -PVP system, an intermediate complex with the formulation (MA)(PbBr) PVP is formed. Within this complex, Br ions partially occupy the coordination sites of Pb^{2} ,

thereby reducing the coordination strength between Pb^{2} and both the C=O and C-N functional groups. Consequently, the C=O and C-N stretching vibrations are shifted to 1656 cm^{1} and 1283 cm^{1}, respectively.

In this study, the Independent Gradient Model based on Hirshfeld partition (IGMH) was employed to visualize the interactions in the PVP-Pb^{2} and DMF-Pb^{2} systems. As can be seen in Fig. 1d, the blue isosurface corresponds to the interaction between Pb^{2} and the carbonyl oxygen of PVP, while the cyan isosurface corresponds to that with the nitrogen atom of the pyrrolidone ring, confirming the presence of two distinct coordination sites. The characteristic blue color of these isosurfaces indicates that the interactions are primarily electrostatic in nature, which is consistent with the FTIR spectroscopic observations. In contrast, the DMF-Pb^{2} system (Fig. 1e) exhibits only a single interaction modality, manifested as a blue isosurface localized at the carbonyl oxygen, indicating a comparatively simpler coordination environment.

To further analyze the thermodynamic properties of DMF and PVP with PbBr , DFT calculations were performed to determine the thermodynamic reaction free energy change (ΔG) (Fig. S1). The results indicate that the binding stability of PVP with PbBr is significantly stronger than that of DMF within the temperature range of 25℃ to 65℃ (298-338 K). At 298 K, the ΔG value for the coordination reaction of PVP-PbBr is -23.48 kcal/mol, which is 13.46 kcal/mol lower than that of the DMF-PbBr system (-10.02 kcal/mol). Notably, the variation in the reaction free energy of PVP-PbBr with temperature (from 298 K to 338 K: +1.20 kcal/mol) is smaller than that of the DMF-PbBr system (from 298 K to 338 K: +1.48 kcal/mol), indicating that the coordination interaction between PVP and Pb^{2} possesses higher thermal stability. This characteristic enables the slow release of Pb^{2} at elevated temperatures, effectively suppressing stray nucleation. This monomer supply regulation mechanism based on thermodynamic equilibrium serves as a critical foundation for the preparation of MAPbBr single crystals with low defect density.

We therefore propose a mechanism for polymer-controlled nucleation and growth of perovskite in solution. Within the metastable zone of crystal growth, the growth rate is determined by two key processes: the transport rate of solutes toward the crystal interface (predominantly diffusion-controlled) and the deposition rate of solutes at the interface [**?**]. To obtain high-quality MAPbBr single crystals, it is necessary to maintain a dynamic equilibrium between the deposition rate at the interface and the solute diffusion rate. As illustrated in Fig. 2a [FIGURE:2], in the conventional ITC method, DMF contains oxygen-coordinating groups that bind to Pb at room temperature, forming the precursor-DMF complex [**?**]. When the temperature increases, DMF dissociates and the solutes diffuse freely in the low-viscosity DMF, promoting rapid nucleation of MAPbBr which tends to induce secondary nucleation. This fast growth process leads to the formation of defects such as dislocations and stacking faults (Fig. 2b). In the precursor solution system with added PVP, the introduction of PVP increases the solution viscosity

while the network structure formed by the long polymer chains hinders solute diffusion.

To further verify the crystalline quality of the obtained samples, structural and optical characterizations were performed. As shown in Fig. S2, the surface of the MAPbBr single crystal (with PVP) appears smoother and more uniform, indicating that the deposition rate of solute at the crystal interface became more homogeneous, thereby suppressing the formation of surface defects. As illustrated in Fig. 3a [FIGURE:3], the XRD signal intensity of the MAPbBr single crystal (without PVP) was measured at 1.3×10 , whereas the MAPbBr single crystal (with PVP) exhibited a significantly enhanced intensity of 8.8×10 . As shown in Fig. 3b, compared to the MAPbBr single crystal (without PVP), the MAPbBr single crystal (with PVP) exhibits decreased full-width-at-half-maximum (FWHM) of the (100) peak, indicating improved crystallinity [**?**].

UV-vis absorption, steady-state photoluminescence (PL), and time-resolved photoluminescence (TRPL) spectroscopy were performed to investigate the optical properties of MAPbBr single crystals. As depicted in Fig. 3c, the absorption spectra of MAPbBr both with and without PVP exhibit a sharp onset near 570 nm. The corresponding Tauc plots yield an identical optical band gap of 2.2 eV, which is consistent with values reported in the literature for MAPbBr single crystals prepared by conventional methods [**?**, **?**]. This indicates that the incorporation of PVP hardly changed the band gap of MAPbBr single crystals. Furthermore, PL spectroscopy was acquired using a combined Raman-fluorescence system (Fig. 3d). Comparative analysis of the spectrum indicates that MAPbBr (with PVP) exhibits a 2.5 nm blue shift in the emission peak relative to MAPbBr (without PVP), accompanied by a significant enhancement in PL intensity and a reduction in the FWHM. These spectral features suggest a decrease in defect state density and inhibition of non-radiative recombination [**?**]. TRPL spectroscopy was further employed to provide direct evidence of improved crystal quality. As depicted in Fig. 3e, the average carrier lifetime of MAPbBr (with PVP) was 47.76 ns, significantly longer than that of MAPbBr (without PVP) (35.31 ns). This notable extension in carrier lifetime indicates a reduction in non-radiative recombination rate and lower defect density, confirming the superior crystalline quality and reduced trap-state density in MAPbBr grown with PVP additive [**?**].

The trap-state density, a critical indicator of crystal quality, was characterized using the SCLC method. Au/MAPbBr /Au devices were fabricated for current-voltage (I-V) measurements. As shown in the typical I-V characteristics, three operational regimes are clearly distinguishable: the Ohmic region, the trap-filled limit (TFL) region, and Child' s region. At low bias voltages, the current follows Ohm' s law, dominated by intrinsic thermally generated carriers. As the voltage increases, a sharp rise in current occurs at the trap-filled limit voltage (V_TFL), indicating saturation of all available trap states. The trap-state density n_trap and carrier mobility can be quantitatively calculated from V_TFL using the following equation [**?**]:

$$n_{\text{trap}} = \frac{2\varepsilon_0 \varepsilon V_{\text{TFL}}}{eL^2}$$

where is the vacuum permittivity (8.85×10^{-12} F/m), is the relative dielectric constant of MAPbBr (=25.5) [**?**], V_TFL denotes the trap-filling limit voltage, e is the elementary charge (1.6×10^{-1} C), and L is the crystal thickness between the electrodes. As shown in Fig. 4a [FIGURE:4] and Fig. 4b, the calculated trap-state densities are 5.38×10 cm^{-3} for MAPbBr (without PVP) and 6.56×10 cm^{-3} for MAPbBr (with PVP). Notably, the trap density of the PVP-modified crystal is substantially lower than those of state-of-the-art semiconductors such as CdTe (10^{11}-10^{13} cm^{-3}) [**?**] and Si (10^{13}-10^{1} cm^{-3}) [**?**]. The MAPbBr (with PVP) exhibits a carrier mobility of 149.7 cm^2/(V · s), which is significantly higher than that of the MAPbBr (without PVP) (88.7 cm^2/(V · s)). The improved carrier mobility, coupled with lower trap-state density, indicates superior crystal quality in the MAPbBr (with PVP), which is essential for high-performance X-ray detection applications.

To assess the X-ray absorption capability of MAPbBr single crystals, the X-ray absorption coefficients of various common materials within the energy range of 1-1000 keV were calculated using the photon cross-section database, as shown in Fig. 4c. The absorption coefficient of MAPbBr is substantially higher than that of conventional silicon, comparable to that of all-inorganic perovskite CsPbBr , and exceeds that of hybrid organic–inorganic perovskite MAPbCl , demonstrating its superior X-ray absorption performance. At a crystal thickness of 1.9 mm, MAPbBr single crystals achieve an attenuation of 96% for 50 keV X-rays, significantly surpassing that of Si (17%) (Fig. 4d). For X-ray detectors, the mobility-lifetime product ( ) is a critical performance metric, which can be derived by fitting the Hecht equation [**?**]:

$$\frac{I}{I_0} = \frac{\mu\tau V}{L^2}\left[1 - \exp\left(-\frac{L^2}{\mu\tau V}\right)\right]$$

where I is the photocurrent, I is the saturation photocurrent, V is the applied voltage, and L is the device thickness. As shown in Fig. 4e and Fig. 4f, the MAPbBr (with PVP) exhibits a product of 1.11×10^{-3} cm^2 · V^{-1}, which is notably higher than that of the MAPbBr (without PVP) (3.63×10 cm^2 · V^{-1}). These results indicate that the PVP-modified crystal possesses superior charge transport properties under X-ray irradiation, demonstrating strong potential for high-performance X-ray detection applications.

The X-ray detection performance of the MAPbBr (with PVP) and MAPbBr (without PVP) single-crystal detectors was characterized. The current density-time (J-t) characteristics of the detectors under X-ray irradiation are shown in Fig. S3. At various bias voltages, both types of detectors exhibit a linear photocurrent response as the X-ray dose rate decreases from 3.0 Gy ·s^{-1} to 24.5 Gy ·s^{-1}. The sensitivity and limit of detection (LOD) were derived from the

current density–dose rate relationships under different biases to quantitatively assess detector performance. The formulas for calculating sensitivity (S) and signal-to-noise ratio (SNR) are as follows [**?**]:

$$S = \frac{J_{\text{photo}} - J_{\text{dark}}}{D}$$

$$\text{SNR} = \frac{\bar{I}_{\text{photo}} - \bar{I}_{\text{dark}}}{\sigma_{\text{photo}}}$$

where D is the X-ray dose rate, J_photo is the current density generated by X-ray, J_dark is the dark current density, Ī_photo is the average photocurrent, Ī_dark is the average dark current, and _photo is the standard deviation of the photocurrent.

The sensitivity under different voltages was obtained by linearly fitting the relationship between current density and X-ray dose rate (Fig. 5a

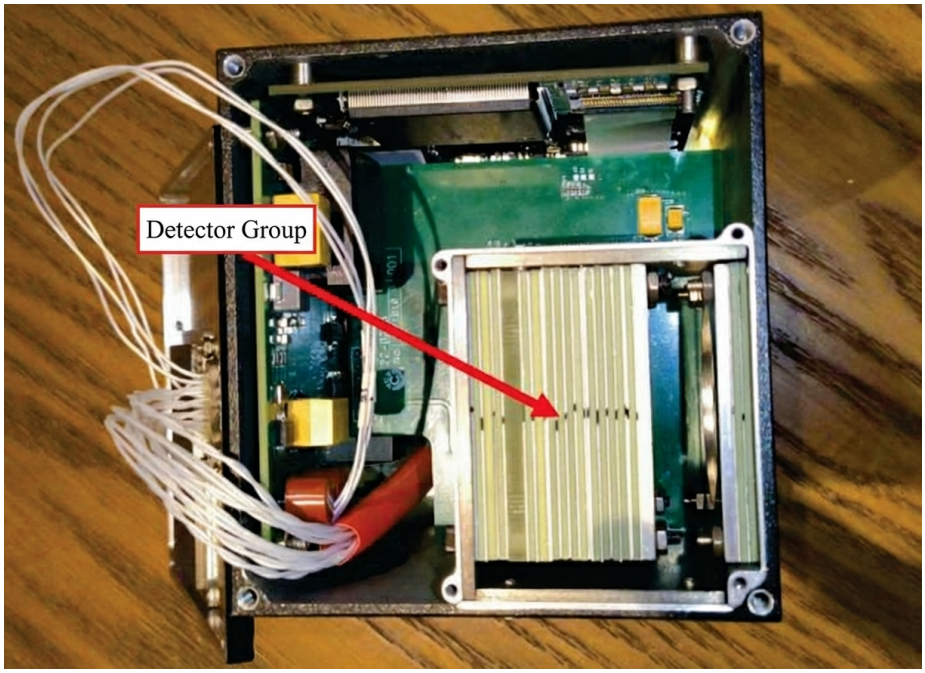

Figure 1: Figure 5

, b). At a bias voltage of 40 V, the detector based on MAPbBr (with PVP) achieved a sensitivity of 1.73×10 C · Gy ^{1} · cm ^{2}, significantly higher than that of the detector using MAPbBr (without PVP) (6495.90 C · Gy ^{1} · cm ^{2}). Furthermore, following the IUPAC definition, the LOD was determined as the

dose rate corresponding to a signal-to-noise ratio (SNR) of 3. As shown in Fig. 5c,d and Fig. S4, the LOD of the detector with MAPbBr (with PVP) single crystal was 43.55 nGy $\cdot s^{-1}$ at 5 V bias, which is substantially lower than that of the detector based on the MAPbBr (without PVP) single crystal (358.27 nGy $\cdot s^{-1}$) and well below the 5.50 Gy $\cdot s^{-1}$ required for medical diagnostic applications [**?**]. A comparison with previously reported MAPbBr X-ray detectors (Fig. 5e and Table S1) confirms the competitive performance of our devices.

Fast response speed is crucial for X-ray imaging applications. The temporal response results (Fig. 5f, g) show that the detector with MAPbBr (with PVP) single crystal exhibits a rise time (10% to 90%) of 0.42 s and a fall time (90% to 10%) of 0.20 s, both shorter than those of the detector with MAPbBr (without PVP) single crystal (0.49 s and 0.25 s, respectively). This improvement results from the higher carrier mobility in the PVP-incorporated crystal, which facilitates more efficient charge extraction.

The X-ray imaging capability of the MAPbBr single-crystal detector is demonstrated in Fig. 6 [FIGURE:6]. The schematic illustration of the X-ray imaging measurements is shown in Fig. 6a. The object is placed between the X-ray source and the detector, and moved by an X-Y scanning manipulator to ensure uniform X-ray exposure across different regions. The X-ray absorption capacity of the object varies depending on its thickness and elemental composition. When the part of the object with high X-ray absorption capacity is exposed to X-rays, less radiation is transmitted, leading to a smaller response current in the detector. Conversely, the detector produces a larger response current when the part with weak X-ray absorption capacity is under exposure. The X-ray imaging capability of the detector was demonstrated using an HEU aperture pattern and a key with intricate internal structures, respectively, under a dose of 3.0 Gy $\cdot s^{-1}$. High-quality images for both objects are clearly revealed in Fig. 6b and Fig. 6c.

The stability of the X-ray detector based on the MAPbBr single crystal was evaluated. In contrast to the rapid performance degradation observed in the device fabricated from the MAPbBr (without PVP) single crystal (Fig. 7a [FIGURE:7]), the device utilizing the MAPbBr (with PVP) single crystal maintained a stable response under a bias of 5 V and a dose rate of 24.5 Gy $\cdot s^{-1}$ for 400 s in ambient conditions, as shown in Fig. 7b.

4. Conclusions

In summary, this study demonstrates that introducing the coordinating polymer PVP into the precursor solution facilitates formation of a "dual-site anchoring" mechanism, providing an effective strategy for controlling perovskite crystallization. IGMH and DFT calculations reveal that the molecular structure of PVP provides dual sites for strong interaction with lead ions, stabilizing the precur-

sor colloids and allowing for controlled release of ions during thermal growth, which optimizes crystal growth kinetics. This strategy yields high-quality single crystals with low defect density, high carrier mobility, short response time, and an impressive product of 1.11×10^{3} $cm^{2}\cdot V^{-1}$. The corresponding X-ray detector exhibits excellent performance, including high sensitivity of 1.73×10 $C\cdot Gy^{-1}\cdot cm^{-2}$ and low LOD of 43.55 $nGy\cdot s^{-1}$. This work provides crucial theoretical guidance and a technical pathway for developing advanced perovskite X-ray detectors.

Funding

This work was supported by the Scientific Research Business Fund Project of Heilongjiang Provincial Research Institutes (No. CZJBKYF2023-02), Specialized Capability Enhancement Project of Heilongjiang Academy of Sciences (No. YSTS2025YZN01), and the Key Project of Research and Development of Heilongjiang Academy of Sciences (No. ZDYF2024YZN01).

References

1. Kim M, Kim H, Sin J, et al., Unveiling the humidity effect and achieving an unprecedented 12% PCE in MAPbBr solar cells. *Chemical Engineering Journal*. (2024). https://doi.org/10.1016/j.cej.2024.154821
2. Chen Y, Peng X, Qin W, et al., Filterless bandpass photodetectors enabled by 2D/3D perovskite heterojunctions. *Advanced Functional Materials* 34 (41), 2403942 (2024). https://doi.org/10.1002/adfm.202403942
3. Wu L, Pan Y, Zhang Y, et al., Violet perovskite quantum dots of MA Bi Br and MA Bi Br Cl synthesized by the Cb-LARP method with tunable emission wavelengths in range of 379-400 nm. *Advanced Functional Materials*. 35(7), 2415315 (2024). https://doi.org/10.1002/adfm.202415315
4. Wang Y, Zhang Q. A characterization study on perovskite X-ray detector performance based on a digital radiography system. *Nuclear Science and Techniques*. 34(5), (2023). https://doi.org/10.1007/s41365-023-01220-4
5. Han J, Li W, Song J, et al., Stable hard X-ray detectors by high-charge-mobility two-dimensional Cu(Gly) Pb Br single crystal. *Energy Letters*. (2024). https://doi.org/10.1021/acsenergylett.4c02866
6. Jiang W, Li H, Xing Z, et al., PEAI surface treatment for low ion migration and high-performance FAPbBr single-crystal X-ray detectors. *ACS Applied Materials & Interfaces*. 16(38), 51630-51638 (2024). https://doi.org/10.1021/acsami.4c09253

7. Qin H, Liu H, Lü Z, et al., New flexible CsPbBr -based scintillator for X-ray tomography. *Nuclear Science and Techniques*. 33(8), 98 (2022). https://doi.org/10.1007/s41365-022-01085-z

8. Han T, Lee J, Choi C, et al., Perovskite-polymer composite cross-linker approach for highly-stable and efficient perovskite solar cells. *Nature Communications*. 10(1), (2019). https://doi.org/10.1038/s41467-019-08455-z

9. Bi D, Yi C, Luo J, et al., Polymer-templated nucleation and crystal growth of perovskite films for solar cells with efficiency greater than 21%. *Nature Energy*. 1(10), 1-5 (2016). https://doi.org/10.1038/nenergy.2016.142

10. Liang A, Feng C, Yang Y, et al., Biomimetic mineralization nucleation with polymer template enabled high-performance perovskite solar cells by anti-solvent-free technology. *Advanced Materials*. 37, 2507401 (2025). https://doi.org/10.1002/adma.202507401

11. Zhao Y, Zhu P, Wang M, et al., A polymerization-assisted grain growth strategy for efficient and stable perovskite solar cells. *Advanced Materials*. 32(17), 1907769 (2020). https://doi.org/10.1016/j.nanoen.2022.107575

12. Zhao J, Wang X, Li Y, et al., Substance discrimination imaging derived from switchable soft and hard X-ray sensing in direct X-ray detector. 7(2), e12632 (2024). https://doi.org/10.1002/inf2.12632

13. Yu F, Song Y, Wang L, et al., Steady-state inverse-temperature crystallization enabling low defect perovskite single crystal efficient X-Ray detectors. *Small*. 21(1), (2024). https://doi.org/10.1002/smll.202407109

14. Su J, Huang Y, Chen H, et al., Solution growth and performance study of Cs AgBiBr single crystal. *Crystal Research and Technology*. 55(3), 1900222 (2020). https://doi.org/10.1002/crat.201900222

15. Li J, Yang Y, Ye Z, et al., Controlled high-quality perovskite single crystals growth for radiation detection: nucleation and growth kinetics of antisolvent vapor-assisted crystallization. *Journal of Materials Science & Technology*. 232, 276-282 (2025). https://doi.org/10.1016/j.jmst.2025.02.019

16. Yu C, Zhang T, Zhou Q, et al., Fast growth of CsPbBr single crystal with high quality by a modified solvent-evaporation method. *Journal of Luminescence*. (2024). https://doi.org/10.1016/j.jlumin.2024.120512

17. Liu Y, Zhang Y, Yang Z, et al., Low-temperature-gradient crystallization for multi-inch high-quality perovskite single crystals record performance photodetectors. *Materials Today*. 22, 67-75 (2019). https://doi.org/10.1016/j.mattod.2018.04.002

18. Xi J, Zhao G, Sun X, et al., Polymer-assisted nucleation for stable single-crystal perovskite thin films. *Chemistry of Materials*. 11(2), e202400478 (2025). https://doi.org/10.1002/cnma.202400478

19. Lu T, Chen Q. Independent gradient model based on Hirshfeld partition: A new method for visual study of interactions in chemical systems. *Journal of Computational Chemistry*. 43(8), (2022). https://doi.org/10.1002/jcc.26812

20. Lu T, Chen F. Multiwfn: A multifunctional wavefunction analyzer. *Journal of Computational Chemistry*. 33(5), 580-592 (2012). https://doi.org/10.1002/jcc.22885

21. Neese F, Wennmohs F, Becker U, et al., The ORCA quantum chemistry program package. *The Journal of Chemical Physics*. 152, 224108 (2020). https://doi.org/10.1063/5.0004608

22. Tirado-Rives J, Jorgensen WL. Performance of B3LYP density functional methods for a large set of organic molecules. *Journal of Chemical Theory and Computation*. 4(2), 297-306 (2008). https://doi.org/10.1021/ct700248k

23. Tsuzuki S, Uchimaru T. Accuracy of intermolecular interaction energies, particularly those of hetero-atom containing molecules obtained by DFT calculations with Grimme' s D2, D3 and D3BJ dispersion corrections. *Physical Chemistry Chemical Physics*. 22, 22508-22519 (2020). https://doi.org/10.1039/D0CP03679J

24. Weigend F. Accurate Coulomb-fitting basis sets for H to Rn. *Physical Chemistry Chemical Physics*. 8(9), 1057-1065 (2006). https://doi.org/10.1039/B515623H

25. Bardakçı T, Kumru M, Altun A. Molecular structures, charge distributions, and vibrational analyses of the tetracoordinate Cu(II), Zn(II), Cd(II), and Hg(II) bromide complexes of p-toluidine investigated by density functional theory in comparison with experiments. *Journal of Molecular Structure*. 1116, 292-302 (2016). https://doi.org/10.1016/j.molstruc.2016.03.023

26. Goerigk L, Grimme S. Efficient and accurate Double-Hybrid-Meta-GGA Density Functionals-Evaluation with the extended GMTKN30 database for General Main Group Thermochemistry, Kinetics, and Noncovalent Interactions. *Journal of Chemical Theory and Computation* 7(2), 291-309 (2011). https://doi.org/10.1021/ct100466k

27. Kilaj A, Gao H, Tahchieva D, et al., Quantum-chemistry-aided identification, synthesis and experimental validation of model systems for conformationally controlled reaction studies: Separation of the conformers of 2,3-dibromobuta-1,3-diene in the gas phase. *Physical Chemistry Chemical Physics*. 22, 13431-13439 (2020). https://doi.org/10.1039/D0CP01396J

28. Vyboishchikov SF, Voityuk AA. Fast non-iterative calculation of solvation energies for water and non-aqueous solvents. *Journal of Computational Chemistry*. 42(17), (2021). https://doi.org/10.1002/jcc.26531

29. Lu T, Chen Q. Shermo: A general code for calculating molecular thermochemistry properties. *Computational and Theoretical Chemistry*. 1200, 113249 (2021). https://doi.org/10.1016/j.comptc.2021.113249

30. Luchini G, Alegre-Requena JV, Funes-Ardoiz I, et al., GoodVibes: automated thermochemistry for heterogeneous computational chemistry data. *F1000Research*. (2020). https://doi.org/10.12688/f1000research.22758.1

31. Yan K, Long M, Zhang T, et al., Hybrid halide perovskite solar cell precursors: colloidal chemistry and coordination engineering behind device processing for high efficiency. *Journal of the American Chemical Society*. 137(13), 4460-4468 (2015). https://doi.org/10.1021/jacs.5b00321

32. Safo IA, Werheid M, Dosche C, et al., The role of polyvinylpyrrolidone (PVP) as a capping and structure-directing agent in the formation of Pt nanocubes. *Nanoscale Advances*. 1(8), 3095-3106 (2019). https://doi.org/10.1039/C9NA00186G

33. Guo Y, Shoyama K, Sato W, et al., Chemical pathways connecting Lead(II) iodide and perovskite via polymeric Plumbate(II) fiber. *Journal of the American Chemical Society*. 137(50), 15907-15914 (2015). https://doi.org/10.1021/jacs.5b10599

34. Zeng S, Xue B, Zhang B, et al., Surface integration modulated low-temperature synthesis for high-quality halide perovskite single crystals. *Chemical Engineering Journal*. (2025). https://doi.org/10.1016/j.cej.2025.163060

35. Liu D, Jiang L, Jiang X, et al., Interface-tension-assisted temperature-gradient crystallization of high-quality MAPbBr perovskite single crystals with low defect densities. *ACS Applied Materials & Interfaces*. 15(49), 57846-57855 (2023). https://doi.org/10.1021/acsami.3c13614

36. Liu D, Sun X, Jiang L, et al., Ultralow detection limit and high sensitivity X-ray detector of high-quality MAPbBr perovskite single crystals. *Journal of Materials Chemistry A*. 12(21), 12467-12474 (2024). https://doi.org/10.1039/D4TA00492B

37. Yu F, Song Y, Wang L, et al., Steady-state inverse-temperature crystallization enabling low defect perovskite single crystal and efficient X-ray detectors. *Small*. 21(1), 2407109 (2025). https://doi.org/10.1002/smll.202407109

38. Liu C, Wang R, Liu J, et al., High-performance self-driven MAPbI - MAPbBr perovskite single crystal heterojunction photodetectors for ultra-sensitive weak light imaging. *Advanced Optical Materials*. 13(11), 2403123 (2025). https://doi.org/10.1002/adom.202403123

39. Saidaminov M, Abdelhady A, Murali B, et al., High-quality bulk hybrid perovskite single crystals within minutes by inverse temperature crystallization. *Nature Communications*. (2015). https://doi.org/10.1038/ncomms8586

40. Balcioglu A, Ahrenkiel R, Hasoon F. Deep-level impurities in CdTe/CdS thin-film solar cells. *Journal of Applied Physics*. 88(12), 7175-7178 (2000). https://doi.org/10.1063/1.1326465

41. Ayres J. Characterization of trapping states in polycrystalline-silicon thin film transistors by deep level transient spectroscopy. *Journal of Applied Physics*. 74(3), 1787-1792 (1993). https://doi.org/10.1063/1.354782

42. Zhao H, Liu N, Li N, et al., Low-Temperature Grown FAPb . Sn . I Single crystals for sensitive X-Ray detectors with low dark current and detection limit. *Advanced Functional Materials*. e17233 (2025). https://doi.org/10.1002/adfm.202517233

43. Xu L, Wang D, Ye H, et al., Ultra-stable and sensitive X-ray detectors using 3D hybrid perovskitoid single crystals. *Small*. 21(9), 2410517 (2025). https://doi.org/10.1002/smll.202410517